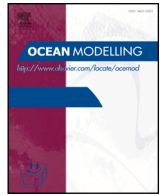




ELSEVIER

Contents lists available at ScienceDirect

Ocean Modelling

journal homepage: www.elsevier.com/locate/ocemod

Virtual Special Issue GoM Virtual Special Issue

A LES-based Eulerian–Lagrangian approach to predict the dynamics of bubble plumes



Bruño Fraga^{a,*}, Thorsten Stoesser^a, Chris C.K. Lai^b, Scott A. Socolofsky^b

^a Hydro-environmental Research Centre, Cardiff School of Engineering, Cardiff University, The Parade CF11 3AA, Cardiff, UK

^b Zachry Department of Civil Engineering, Texas A&M University, 3136 TAMU, College Station, TX 77843-3136, USA

ARTICLE INFO

Article history:

Received 9 June 2015

Revised 3 October 2015

Accepted 1 November 2015

Available online 10 November 2015

Keywords:

Bubble plumes

Large-eddy simulation

Lagrangian Particle Tracking

Two-way coupling

Slip velocity

Delta functions

ABSTRACT

An approach for Eulerian–Lagrangian large-eddy simulation of bubble plume dynamics is presented and its performance evaluated. The main numerical novelties consist in defining the gas–liquid coupling based on the bubble size to mesh resolution ratio (D_p/Δ_x) and the interpolation between Eulerian and Lagrangian frameworks through the use of delta functions. The model's performance is thoroughly validated for a bubble plume in a cubic tank in initially quiescent water using experimental data obtained from high-resolution ADV and PIV measurements. The predicted time-averaged velocities and second-order statistics show good agreement with the measurements, including the reproduction of the anisotropic nature of the plume's turbulence. Further, the predicted Eulerian and Lagrangian velocity fields, second-order turbulence statistics and interfacial gas–liquid forces are quantified and discussed as well as the visualization of the time-averaged primary and secondary flow structure in the tank.

© 2015 The Authors. Published by Elsevier Ltd.

This is an open access article under the CC BY license (<http://creativecommons.org/licenses/by/4.0/>).

1. Introduction

There are many engineering applications of bubble plumes within a carrier liquid, such as fermentation devices, bubble reactors, boilers or nuclear reactors. Several important environmental and ocean engineering examples include destratification and aeration of lakes or reservoirs (e.g. Asaeda and Imberger, 1993; Sahoo and Luketina, 2003; Wüest et al., 1992), the injection of CO₂ in the deep ocean (e.g. Caulfield et al., 1997; Socolofsky and Adams, 2002) or gas releases from natural vents or accidental well blow-outs (e.g. Fabregat et al. (2015) (this issue); Socolofsky and Adams, 2003; Yapa et al., 1999). Recent work has provided new insights on the integral or bulk properties of the mixture (e.g. Bombardelli et al., 2007; Socolofsky and Adams, 2005; Socolofsky et al., 2008) and also reported on the local turbulent flow field and its statistical properties (e.g. Martínez Mercado et al., 2010; Mazzitelli and Lohse, 2009). However, the accurate prediction or reproduction of bubble plumes has been a challenging task for both Computational Fluid Dynamics (CFD) modellers and experimentalists.

The 3D numerical modelling/simulation of bubbly flows requires accurate treatments of the carrier and dispersed phases as well as the coupling and interaction between the two. The flow and turbulence of the carrier phase can be categorized into: (1) numerical resolution of all turbulent scales, i.e. Direct Numerical Simulation (DNS), (2) numerical resolution of only the largest and most energetic eddies and subgrid-scale modelling of the small scales, i.e. Large Eddy Simulation (LES) or (3) modelling of the entire turbulent spectrum through a turbulence model and solving for the time-averaged flow only, i.e. Reynolds-Averaged Navier–Stokes simulation (RANS). The latter was the most common approach to calculate bubble plumes until the last decade, due to its relatively low computational requirements (see Becker et al., 1994; Laín et al., 2002; Sato and Sekoguchi, 1975; Sokolichin et al., 1997). RANS rely on closure models to account for the unsteadiness in the flow. However, even at a low Reynolds number of the liquid phase, bubbles induce significant turbulence (also called pseudo-turbulence) of anisotropic nature (see Dhotre et al., 2013), contrasting with the main assumption (isotropic turbulence) of most RANS turbulence closure models. DNS is the most accurate approach to predict bubble plume dynamics, but its high cost prevents it from being employed for many practical applications. Hence DNS is considered a tool for fundamental research on the physics of the liquid–bubble interaction

* Corresponding author. Tel.: +447472029663.

E-mail address: FragaB@cardiff.ac.uk, brunhofraga@gmail.com (B. Fraga).

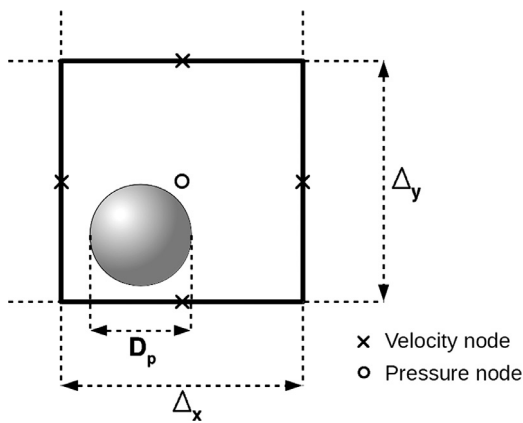


Fig. 1. Relation between the bubbles' size D_p and the grid resolution Δx .

(e.g. Bunner and Tryggvason, 2002) or to produce highly accurate data for the validation for more macroscopic approaches (e.g. Bestion, 2012). LES is a promising compromise between accuracy and applicability and it has received some attention in recent years. However, whilst LES has been applied successfully for many single-phase flows (e.g. Rodi et al., 2013; Stoesser, 2014), many challenges remain with regards to the treatment of the dispersed phase in multiphase flows.

Three main methods exist to simulate the gas bubbles and to couple it with the liquid, namely (1) Eulerian–Eulerian (EE), i.e. both the carrier phase and the gas phase are computed in an Eulerian framework, (2) Eulerian–Lagrangian (EL), i.e. the carried liquid is calculated as in (1) and the gas phase is treated as Lagrangian markers, and (3) Interface Tracking (IT), i.e. the carried liquid is calculated as in (1) and some features of the interface between liquid and gas phases are resolved by the numerical method. EE has the great advantage of low computational cost compared to EL or IT because the gas phase is calculated efficiently by solving only one additional transport equation. With this method, a two-phase flow is simulated, assuming that the gas phase is continuous and that liquid and gas interpenetrate each other. Milelli et al. (2001) studied the role of the ratio of particle-to-mesh size $D_p/\Delta x$ (see Fig. 1), the influence of the subgrid scale (SGS) model and the role of the lift coefficient in EE; Deen et al. (2001) and Dhotre et al. (2009) compared RANS and LES predictions; Ničeno et al. (2009) analysed the importance of SGS modelling and the bubble-filter ratio; Ma et al. (2014) compare the results obtained with EE-LES, EE-URANS, EL-LES and experiments and provide a method to include the contribution to the SGS turbulence generated by the unresolved scales; Fabregat et al. (2015) studied the evolution of thermal and gas plumes in stratified environments with a spectral solver. The review by Dhotre et al. (2013) provides a good summary of the success and limitations of EE. There are some drawbacks of the EE approach though, which are the inherent numerical diffusion of the Eulerian treatment of the bubble-phase (which can be mitigated by the use of high-order discretization schemes (Sokolichin et al., 1997)) and the lack of physical details of the bubble dynamics and carrier-fluid-bubble interaction. The assumption of a filter size considerably larger than the size of the bubbles (so they can be considered continuous when they are actually discrete) prevents this method from solving the turbulence generating scales close to the order of the bubble size (Ma et al., 2014).

IT approaches are on the other side of the numerical methods spectrum, being the most accurate approach to a bubbly flow but also the most expensive. Different IT techniques have been developed such as Level Set (Sussman et al., 1994), Volume of Fluid (Hirt and Nichols, 1981), Front Tracking (Unverdi and Tryggvason, 1992) or Constrained Interpolation Profile (Yabe et al., 2001). All of

them solve the interfacial interactions between the dispersed face and the carrier fluid without or with only minimum semi-empirical closure. In order to track accurately the gas-liquid interface, IT-LES requires a high filter width ratio ($D_p/\Delta x \approx 20$), which results in high resolution of the liquid phase, and hence most IT simulations don't require sgs-modelling anymore. IT methods face the challenge of the proper implementation of boundary conditions between the two phases but the main drawback is the extremely high computational cost, making it feasible for only a low number of bubbles and for flows at low Reynolds numbers. IT methods are extremely useful for the understanding of the underlying physical mechanisms of the fluid-bubble interactions but should be considered complementary to other, more practical approaches of engineering interest (Mazzitelli and Lohse, 2009). An important aspect of the physics predicted by bubble-resolved simulations is the generation of bubble-wake-induced turbulence which usually adds to the carrier liquid energy cascade and which is reflected in the energy spectrum. For instance, physical modelling and some recent IT-DNS suggest the slope of the energy cascade to be -3 instead of the $-\frac{5}{3}$ for homogeneous turbulence (see Martínez Mercado et al., 2010; Roghair et al., 2011). Some examples of IT simulations that involve more than one single bubble are: Bunner and Tryggvason (2002), DNS with up to 216 bubbles; Esmaeili and Tryggvason (1998), DNS with up to 49 bubbles; Lu et al. (2005), DNS with 16 bubbles; Roghair et al. (2011), DNS with 16 bubbles or Yujie et al. (2012), DNS up to approx. 50 bubbles.

Eulerian–Lagrangian based Large-Eddy Simulation (EL-LES) sits somewhere between EE and IT and it employs Lagrangian Particle Tracking (LPT) to simulate the dispersed phase. Each bubble is represented by a Lagrangian point which moves across the Eulerian mesh according to the Newton's second law of motion. Compared with EE, EL gives detailed information about every bubble's position, force and velocity, and this method may allow more flexibility in the $D_p/\Delta x$ ratio. In their pioneering work in 1997, Sokolichin et al. (1997) applied EE and EL to a bubble column previously studied experimentally (Becker et al., 1999). They concluded that, with the appropriate non-diffusive convection schemes, EE could be as accurate as EL when predicting the average flow structure. No turbulent properties were investigated. EL-LES is more expensive than EE-LES because each particle requires the calculation of a set of equations and a mapping procedure between the Lagrangian and Eulerian coordinates. Compared to IT, EL is less costly (lower resolution, lower $D_p/\Delta x$ and broader assumptions) and offers wider applicability, being able to deal with much larger number of particles and higher Reynolds numbers. On the other hand, the bubble-liquid interface is not resolved and the method relies on semi-empirical formulae to compute acting bubble forces.

Despite its advantages, EL-LES faces the overarching issue regarding the optimum $D_p/\Delta x$. Some authors apply the constraint suggested by Milelli et al. (2001) for EE $D_p/\Delta x < 0.67$ with some flexibility. A slightly smaller Δx can provide a better compromise between capturing the most energetic eddies and the aforementioned criterion (e.g. Sungkorn et al., 2011). Some authors developed variations of EL to deal with a wide range of sizes, such as the PSI-ball (particle-source-in-ball) approach (Hu and Celik, 2008). The basic idea behind this formulation is the creation of an influence volume (ball) around the bubble (in Hu and Celik (2008) a sphere of $2D_p$ diameter is suggested). All the Eulerian nodes within this volume will receive a contribution from the bubble that originates the ball. As the ball's size depends on the particle's dimension, this method should be able to deal with a wide range of values for D_p , specially for large $D_p/\Delta x$ cases. This method was named in contrast with the particle-source-in-cell (PSI-cell) method developed by Crowe et al. (1977), in which only the host cell in which the centroid of the bubble is located is affected by its presence. The Eulerian–Lagrangian treatment of bubble plumes has not been restricted to LES, as there are

successful experiences with RANS (Láin et al., 2002) and DNS (e.g. Kitagawa et al., 2001; Mazzitelli and Lohse, 2009).

In this paper a refined Eulerian–Lagrangian LES approach is proposed, introducing a new LPT algorithm and a revised formulation of the PSI-ball method. The model's performance is evaluated quantitatively in terms of first and second order statistics using high-resolution experimental data. The comparison with ADV results and the use of different mesh resolutions allows for insightful discussions to what extent large-scale turbulence can be resolved through an EL-LES method. Furthermore, the paper provides important bubble plume details which EL-LES can deliver such as the distribution of the slip velocity, the balance of forces on a bubble within the plume, the description of the secondary flow in the tank or the revelation of instantaneous turbulence structures in the plume.

2. Numerical framework

The in-house finite-difference-based Large-Eddy Simulation code Hydro3D is employed. Hydro3D solves the filtered Navier–Stokes equations on staggered grids for the continuous (liquid) phase and has been validated thoroughly for many different flows (e.g. Bomminayuni and Stoesser, 2011; Bai et al., 2013; Kara et al., 2015; 2012; Kim and Stoesser, 2011; Kim et al., 2013; Papanicolaou et al., 2012). The code is equipped with a Lagrangian Particle Tracking algorithm to allow for accurate predictions of the dispersed (bubbles) phase, the validation of which is the subject of this work.

2.1. Continuous phase

Hydro3D solves the space-filtered mass and momentum conservation equations for an incompressible fluid:

$$\frac{\partial u_i}{\partial x_i} = 0 \quad (1)$$

$$\frac{\partial u_i}{\partial t} + \frac{\partial u_i u_j}{\partial x_j} = -\frac{\partial p}{\partial x_i} + 2\nu \frac{\partial (S_{ij})}{\partial x_j} - \frac{\partial \tau_{ij}}{\partial x_j} + \xi_i \quad (2)$$

where u_i refers to the velocity component in the spatial direction i , t is the time, p the pressure, ν the dynamic viscosity and S_{ij} the strain rate tensor. The term τ_{ij} accounts for the unresolved turbulence, which is calculated through the turbulent viscosity ν_t using the Smagorinsky sub-grid scale (SGS) model. The Smagorinsky constant C_S is set to $C_S = 0.1$ for all simulations. ξ_i is a source term and accounts for the contribution of the dispersed phase to the flow. The derivatives in the governing equations are discretized with a three-step Runge–Kutta algorithm for the time derivative and second-order central differencing schemes for both convective and diffusive terms. The code is based on a predictor-corrector fractional step method with the solution of the Poisson pressure equation using a multi-grid method as the corrector.

2.2. Dispersed phase

In Eulerian–Lagrangian simulations the bubbles are represented by volumeless Lagrangian points/markers. The physical effect of the interphase liquid–gas is modelled through the forces described in this section. The assumptions made for this case are that the bubbles are rigid and spheric and that there is no direct interaction between them (due to the relatively dilute gas mixture). Also only linear interaction between interfacial forces is considered. The motion of individual bubbles (from here onwards called particles) is computed by Newton's second law:

$$m_p \frac{\partial v_{p,i}}{\partial t} = F_{p,i} \quad (3)$$

where m_p is the particle's mass, $v_{p,i}$ is the particle's velocity in spatial direction i and $F_{p,i}$ is the sum of the interfacial liquid forces acting on the particle in direction i . The integral forces acting on each particle are approximated by semi-empirical formulae. The following five forces are considered (Delnoij et al., 1997): buoyancy, fluid stress, added mass, drag and lift. The buoyancy force is computed as:

$$F_{G,3} = (m_p - m_l)g \quad (4)$$

where m_l is the displaced liquid mass and g is the acceleration due to gravity. The buoyancy force applies only in the vertical direction $i = 3$. The fluid stress force, which accounts for part of the fluid's resistance to the particle's acceleration, is computed as:

$$F_{S,i} = m_l \frac{Du_i}{Dt} \quad (5)$$

where u_i is the fluid velocity at the bubble's geometric center location. The added mass force, which represents the fluid's resistance to the particle's movement which is dependent of the slip velocity, reads:

$$F_{A,i} = -C_A m_l \frac{\partial}{\partial t} (v_{p,i} - u_i) \quad (6)$$

where C_A is an empirical coefficient, assumed to be 0.5 for a sphere (Delnoij et al., 1997) and the difference between particle and water velocity ($v_{p,i} - u_i$) is often referred to as the slip velocity u_{slip} . The drag force, which is exerted by the particle on the liquid (and vice versa) in the direction of motion, is computed as:

$$F_{D,i} = \frac{1}{2} C_D \rho A_{fr} |v_{p,i} - u_i| (v_{p,i} - u_i) \quad (7)$$

where A_{fr} is the frontal area of the particle and ρ the fluid density. The drag coefficient C_D depends on the local Reynolds number Re_p and is calculated from the standard drag curve (Clift et al., 1978):

$$C_D = \begin{cases} \frac{24}{Re_p} (1 + 0.15 Re_p^{0.687}) & Re_p \leq 800 \\ 0.44 & Re_p > 800 \end{cases} \quad (8)$$

The lift force, which is the force exerted on the particle perpendicular to the axis of motion and which is responsible for the particles spreading is computed as:

$$F_{L,i} = -C_L m_p (v_{p,i} - u_i) \times \omega_i \quad (9)$$

where ω_i is the fluid vorticity and $C_L = 0.53$ is the lift coefficient for a sphere.

2.3. Eulerian–Lagrangian mapping: a refined approach

In a two-way coupling approach, as is proposed here, exchange of information is required twice. First, the interfacial particle forces are calculated from Eqs. (4)–(9) and through Eq. (3) the particles' velocities are obtained. This is called forward coupling. Second, the contribution of the dispersed phase to the continuous one is computed and added as a source term, ξ , to the liquid's momentum Eq. (2). This is called reverse or backward coupling. Forward and backward coupling is achieved by connecting randomly placed Lagrangian particles with fixed Eulerian framework and this is achieved through a mapping technique. Mapping consists of two basic elements: (1) the definition of the volume of fluid influenced by the particle and (2) interpolation techniques to transfer quantities between Eulerian and Lagrangian frameworks.

Focusing on element (1), the starting point for this work is the aforementioned PSI-ball approach developed by Hu and Celik (2008). Two main novelties are incorporated: (a) the size of the influence volume (which is a cube instead of a sphere) depends on the $D_p/\Delta x$ ratio rather than only on D_p ; (b) for the sake of consistency the chosen volume of influence is used for both forward and backward coupling. As in two-way coupling both phases affect dynamically each other, the

influence radius for both should be the same. Besides, this procedure is more efficient computationally. Regarding a), the size of the influence volume is defined by $R = k \cdot h$, where R is the length of the edge of the influence cube, k is a constant (typically 3, 4 or 5) which depends on the choice of interpolation function (commented later in this section) and h is defined by Eq. 10:

$$h = \begin{cases} \Delta x & \frac{D_p}{\Delta x} \leq 1 \\ D_p & \frac{D_p}{\Delta x} > 1 \end{cases} \quad (10)$$

This procedure ensures the accuracy of the interpolation with a large enough representation of points, even for low $D_p/\Delta x$. The classic PSI-ball method ($2D_p$ -sized ball) can lead to under-representation of points when $D_p/\Delta x$ is smaller than 1, as illustrated in Fig. 2. This sketch represents this mesh dependency in a 2D application of the classic PSI-ball method for two different grid resolutions (left is twice as fine as right). For the fine grid bubbles A and B influence four velocity nodes (crosses) each. However, for the coarse mesh (right), bubble A only gets two nodes inside the ball and bubble B would have no force interaction with the liquid flow.

With regards to element 2) of the mapping, transfer of quantities, this has been a major aspect for CFD modellers. Some examples are cited: Delnoij et al. (1997) proposed an area-weighted averaging; Laín et al. (2002) suggested linear interpolation plus a fluctuating component; Kitagawa et al. (2001) used a box or Gaussian template function; Deen et al. (2004) chose a clipped fourth-order polynomial kernel, which was also used by Darmana et al. (2006) and Sungkorn et al. (2011) and Hu and Celik (2008) chose a truncated Gaussian for the forward coupling whilst applying a distance weighted function for the backward coupling.

In here the smoothed delta functions developed by Yang et al. (2009) are chosen. This family of second-order polynomial functions has been specifically designed to transfer Eulerian-to-Lagrangian quantities and successfully applied in recent years within immersed boundary problems, which hold similarities with Lagrangian Particle Tracking. In both there are discrete forcing points which do not coincide with the Eulerian grid nodes and hence transferring forces between different frames of reference is a key element. The smoothed version of the discrete delta functions significantly reduce the amount of non-physical 'noise' generated in the interpolation (Yang et al., 2009). The general expression of the three-dimensional delta function is as follows:

$$\delta(\mathbf{x}_p - \mathbf{x}_j) = \frac{1}{h^3} \phi\left(\frac{x_p - x_j}{h}\right) \phi\left(\frac{y_p - y_j}{h}\right) \phi\left(\frac{z_p - z_j}{h}\right) \quad (11)$$

where δ is the 3D delta function, h is the stencil size (defined in 10), the subscript j refers to the cell nodes and p to the particles/bubbles. In the present work, the smoothed 4-point piecewise function $\phi = \phi_4^*$ was chosen. This implies that $k = 5$, giving a cubic influence volume whose edge's length comprises 5 Eulerian cells (if $D_p/\Delta x \leq 1$) or more (if $D_p/\Delta x > 1$). This delta function creates a 3D Gaussian-like kernel centred in the Lagrangian point, so the nodes that are distant or near the corners of the resulting cube will have tiny influence or none.

Delta functions provide accurate results for the Eulerian–Lagrangian interpolation (step 6 of Alg. 1), unfortunately they are not suitable for the Lagrangian–Eulerian step (step 9). They require the collection of points to be regularly arranged, which is not usually the case of the bubbles within the gas plume. A volume-average was applied instead, hence the contribution of every particle over an Eulerian node is multiplied by a term $\Delta V = \frac{V_p}{V_{ball}} \frac{L_j}{L_k}$, being V_p the volume of the bubble and V_{ball} the volume of the influence region and $\frac{L_j}{L_k}$ is a distance weighted linear function that ensures those particles which are closer to the considered node have a bigger impact, in the same way that was suggested in Hu and Celik (2008).

Algorithm 1 Lagrangian Particle Tracking Algorithm.

for $t=1, t_{end}$ do

Time step loop

Note: the first three steps take place only in the master processor

1. **Removal.** Bubbles that have reached the water surface during the previous time step are removed and the others are renumbered.

2. **Release.** A new set of particles is released in consistency with the prescribed flow rate and added to the updated pool of bubbles.

3. **Scatter.** The master processor distributes the bubbles among the other processors according to their location using the MPI-SCATTERV directive.

Note: from this point, the steps will run in parallel in all processors with particles

for $L = 1, M$ do

Loop in particles. OpenMP parallelization

4. **Location.** Bubble p is tracked within the domain and the closest velocity and pressure nodes are located.

5. **Influence volume.** Depending on the stencil h and the interpolation order, the N Eulerian nodes which will interact with the bubble are selected.

6. **Eu-Lag interpolation.** 3D Eulerian velocities from the previously defined nodes are interpolated at the location of the bubble:

$$u_i = \sum_{j=1}^N u_{j,i} \delta(x_{p,i} - x_{j,i})$$

7. **Forward coupling (Liquid-Gas).** Slip velocity is calculated based on the Lagrangian velocities of the previous time step using an implicit form of Eq. 3 and considering $F_{p,i} = F_{G,3} + F_{S,i} + F_{A,i} + F_{D,i} + F_{L,i}$:

$$v_{p,i}^t = v_{p,i}^{t-1} + \Delta t \left[3 \frac{u_{slip}}{\Delta t} - \frac{3}{2D_p} C_d |u_{slip}| u_{slip} - 2C_L u_{slip} \times \omega_i^{t-1} \right]$$

8. **Backward coupling (Gas-Liquid).** Updated Lagrangian velocities are used to calculate the reaction force by volume unit. The buoyancy force is not included because the impact of gravity on the carrier fluid is already accounted for in the momentum equations:

$$F_{p,i}^* = [F_{S,i} + F_{A,i} + F_{D,i} + F_{L,i}]$$

9. **Source terms calculation.** Backward forces are added to the source terms of the nodes within the influence volume:

$$\xi_i = -\frac{1}{V_p} \sum_{p=1}^M F_{p,i}^* \Delta V$$

end for

10. **Momentum equations.** Source terms are added to the Eulerian momentum equation (Eq. 2).

11. **Actualization.** Bubbles' locations are updated.

12. **Gather.** Relevant updated information of every bubble is sent to the master processor using the MPI-GATHERV directive.

end for

2.4. Eulerian–Lagrangian coupling algorithm

The calculation procedure for every time step of the described method is described in Algorithm 1. Indexes j , p and i account for Eulerian nodes, Lagrangian markers and Cartesian velocity components respectively; M is the total number of particles; N the nodes in the influence volume.

3. Model performance assessment: boundary conditions and setup

The model's performance is evaluated by predicting the dynamics of the bubble plume that was studied experimentally in the Fluid Dynamics Laboratory in the Zachry Department of Civil Engineering

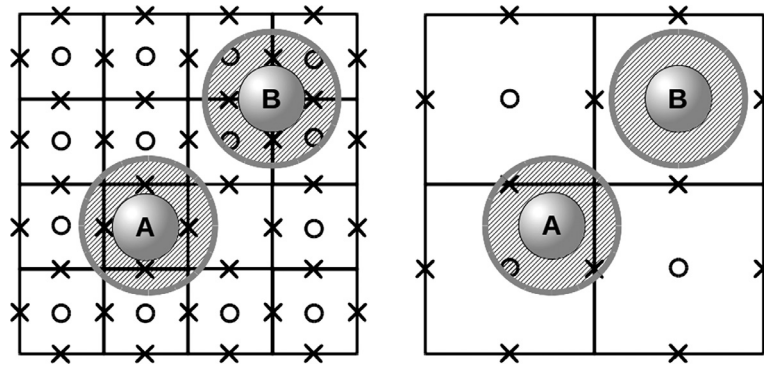


Fig. 2. Influence of the grid resolution on the Lagrangian–Eulerian mapping through PSI-ball.

at Texas A&M University. The setup of the experiment is sketched in Fig. 3. Compressed air was injected at a constant gas flow rate of $Q_g = 0.5l/min$ at standard conditions through an aquarium airstone located at the bottom of a 1 m wide, 1 m deep cubic tank creating bubbles with a diameter between 2–4 mm and a median size of 2.4mm. High-resolution velocity data were measured using Acoustic Doppler Velocimetry (ADV) with a Nortek Vectrino II velocity profiler at different elevations above the injections. More details of the experiment are reported in Lai (2015). Also, Particle Image Velocimetry (PIV) measurements were conducted previously for the same setup and conditions, as specified in Bryant et al. (2009). The ADV datasets used in the present work have been corrected using the method proposed in Hurther and Lemmin (2001). A sufficiently long sampling time of 15–18 min was used during the experiments so that well-converged second-order statistics could be obtained minimizing the random sampling errors. Both datasets are used for validation purposes in this section, although the main reference is the more recent and higher resolution ADV measurements.

The numerical simulations are carried out under analogous conditions to the experiment. The boundary conditions for the dispersed phase are the prescription of a gas flow rate of $Q_g = 0.5l/min$ and a bubble diameter of $D_p = 2mm$. Bubbles are initially randomly distributed over the release area and once they make their way through the tank and reach the water surface they are removed from the computational domain. The average number of bubbles for a fully developed bubble plume is approximately 6000. Boundary conditions for the continuous phase include the use of the no-slip boundary condition at all solid walls and a rigid lid at the water surface with a free slip condition. Three different uniformly spaced grids are em-

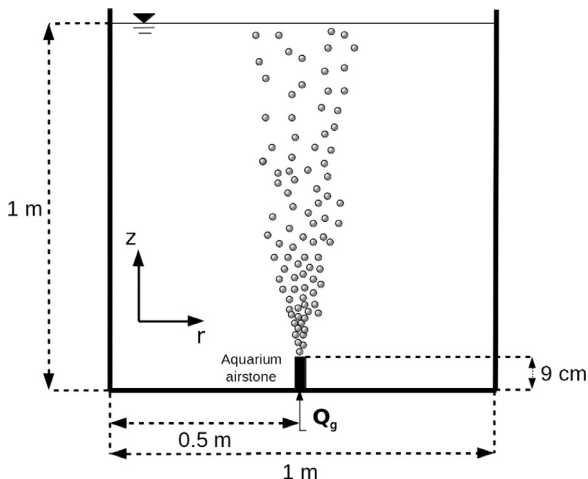


Fig. 3. Side view of the experimental setup.

Table 1

Bubble-to-mesh size ratio for the three mesh resolutions tested and Milelli's proposed limit of applicability (Milelli et al., 2001).

	Coarse mesh	Medium mesh	Milelli's limit	Fine mesh
$D_p/\Delta x$	0.32	0.64	0.67	0.8

ployed for the simulations: $\Delta x = 6.25mm$, $\Delta x = 3.125mm$ and $\Delta x = 2.5mm$, yielding a total number of gridpoints of 4Mio, 32.7Mio and 64Mio, respectively. The mesh resolutions are chosen with Milelli's recommendations in mind, as illustrated in Table 1. The size of the medium mesh ($\Delta x = 3.125mm$) is very close to Milelli's proposed limit, the fine grid ($\Delta x = 2.5mm$) exceeds it and the coarse grid is considered reasonably fine to effectively resolve explicitly large-scale turbulence.

The code is executed using a hybrid parallelization method. The finest grid employed 125 MPI tasks on Cardiff University's high-performance computer facilities. The particles' advection between domains is accomplished using standard MPI commands as described in Alg. 1. For approx. 6,000 bubbles, the LPT calculation comprise 60% of the total computational load. By using 4 OpenMP threads on those processors with significant amounts of bubbles, the CPU time spent per time step can be cut in half.

4. Model validation: results and discussion

In the first instance the results of the medium mesh simulation are used to assess the performance of the code, while mesh size sensitivity is investigated afterwards. The reference frame is Cartesian, being X and Y the horizontal axis and Z the vertical one. Some of the flow properties presented in the following are plotted as a function of the dimensionless radial distance from the plume center line $\frac{r}{b_v}$. The plume's width scale b_v is the distance between the plume center and the point where $W(b_v) = e^{-1}W_c$, where W_c is the time-averaged vertical velocity at the plume's center line. Furthermore, some of the numerical/experimental results are plotted at non-dimensional depth z/D , where D is the scale which characterises the length of the more energetic eddies in the bubble plume. D was first defined by Bombardelli et al. (2007) and since then has been used as the principal length scale of a bubble plume by many experimentalists and modellers. D is calculated as:

$$D = \frac{gQ_g}{4\pi\alpha^2w_{slip}^3} \quad (12)$$

where Q_g is the air-volume inflow at atmospheric pressure, α is the plume entrainment coefficient (here $\alpha = 0.1$) and w_{slip} is the slip velocity (approx. 20 cm/s on average for this case, as reported in Section 4.1). For the case considered in this study $D = 8.1$ cm. All the numerical radial profiles presented in this section are the result of

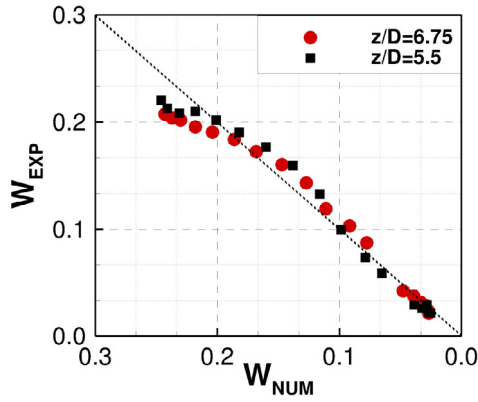


Fig. 4. Numerical versus experimental time-averaged vertical velocities of the entrained fluid inside the bubble plume at $z/D = 5.5$ (black squares) and $z/D = 6.75$ (red circles).

integrating the predicted results around the center of the plume at the considered height.

4.1. Time-averaged stream-wise velocity of the continuous phase

Fig. 4 presents simulated (W_{NUM}) and ADV-measured (W_{EXP}) time-averaged vertical fluid velocities at identical radial locations for two different depths, i.e. $z/D = 5.5$ (squares) and $z/D = 6.75$ (circles), between the plume center and $r = 2b_v$. The overall agreement is quite good, but there is a slight over-prediction of the experimental velocities near the plume's centerline. The main reason for that may be the fact that the simulations were carried out with 2 mm bubbles, whereas in the experiments there is a narrow range of sizes, with a 2.4 mm average diameter and smaller bubbles generate higher centerline velocities.

Fig. 5 plots profiles of the numerically predicted non-dimensional time-averaged vertical velocity of the liquid at $z/D = 5.5$ and $z/D = 6.75$ and the ADV results of those locations together with the generally accepted Gaussian self-similar velocity distribution $W(r)/W_c = \exp(-r^2/b_v^2)$. The simulated profile shows an almost perfect agreement with both the experiments and the theoretical model. There is a discrepancy with the Gaussian curve from approx. $r/b_v > 1.4$. There the velocity predicted by the theoretical model is underestimated because the self-similar model does not consider the returning flow generated in a confined geometry, while both experiments and simulation do.

Fig. 6 represents the three main zones that constitute the bubble plume: (A) a core region characterised by the high density of particles, (B) the transition zone where gas fraction decreases abruptly

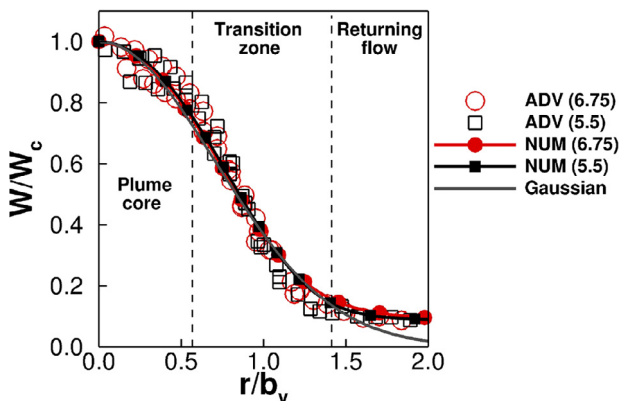


Fig. 5. Gaussian fit of the dimensionless velocity profile of the entrained fluid inside the plume at $z/D = 5.5$ (black squares) and $z/D = 6.75$ (red circles).

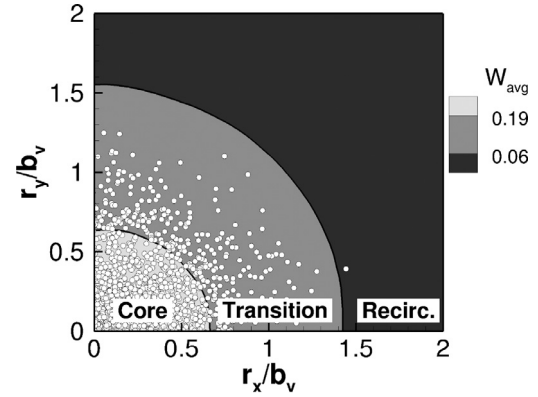


Fig. 6. Time-averaged vertical velocity contour lines of the entrained fluid at $z/D = 5.5$ in one quarter of the plume.

and the gradients are high and (C) an area without bubbles (except from some eventual wandering particle) which is characterized by the circulating tank flow.

4.2. Second-order statistics of the continuous phase

Fig. 7 compares data from the numerical simulations with experimental measurements for second-order non-dimensional turbulence statistics at $z/D = 5.5$ and $z/D = 6.75$. In this case, both ADV and PIV data are displayed, although the PIV measurements only reach until $r/b_v = 1.5$. The overall trend is very well captured, but the quantitative agreement varies depending on the property. The numerically predicted vertical turbulent fluctuations w_{rms}/W exhibit a good agreement with PIV results but a constant deviation in magnitude from the ADV data, in particular at the plume's core and in the transition zone. It seems that EL-LES approach is unable to resolve all the turbulence generated at the bubble scale (e.g. flow separation at the interface, vortex shedding and hence local interaction of wakes), as the method does not intend to solve explicitly the gas-liquid interface (Mazzitelli and Lohse, 2009). The PIV dataset lacks the sufficient resolution to capture small-scale turbulence. This suggests that a more sophisticated large-eddy simulation closure model may be needed, possibly to add bubble-induced turbulence production to the SGS-model (Ma et al., 2014). As the ADV measurements show, the bubbly flow is strongly anisotropic, with a clear dominance of turbulence in the vertical streamwise direction. It is worth noting that whereas the PIV results are almost isotropic, the simulations are not. The peak for the predicted vertical fluctuations is a 25% higher than for the horizontal ones. Hence, some of the relevant turbulent scales are actually solved (e.g. oscillations in the motion of individual bubbles, clustering of particles or interactions between trajectories). This makes a key difference with the results provided by models with isotropic closure (eg. RANS plus $k - \epsilon$) or those that are only applicable at fairly low $D_p/\Delta x$ values.

The numerical-ADV agreement for the horizontal (u_{rms}/W) fluctuations and the turbulent shear stress (uw_{rms}/W^2) is very good. There may be a very small difference on the location of the main peaks of the profiles which can also be due to the difference in the bubble size distributions of experiments and simulations. But the overall agreement is remarkable. The coincidence with PIV is very good as well, both in the evolution from the plume's core and the peaks' locations.

4.3. Slip velocity and tracking of Lagrangian forces

The left side of Fig. 8 shows the distribution of the time-averaged (using 50,000 time steps) vertical slip velocity W_{slip} in the symmetry plane. The distribution appears to be relatively constant with sharp gradient at the plume's edge. A more quantitative view is provided

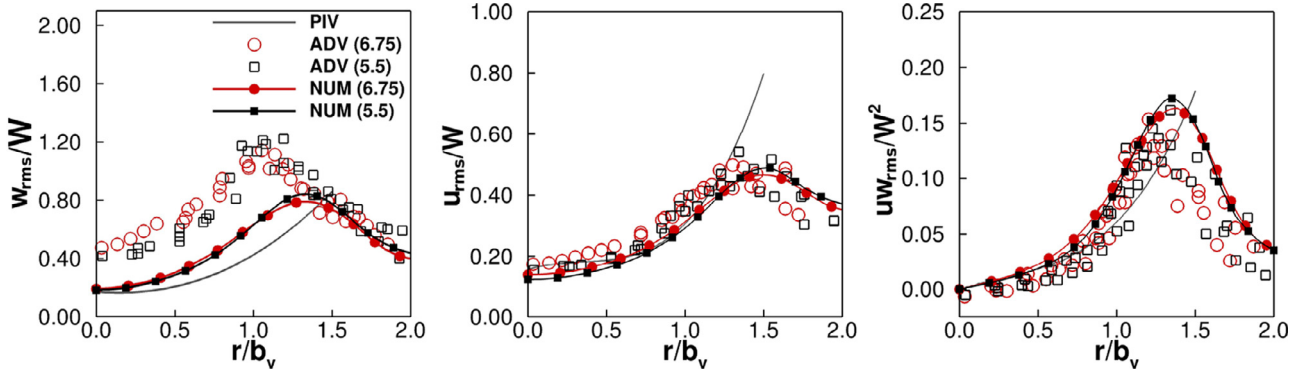


Fig. 7. Turbulent Reynolds stresses for numerical (lines with solid symbols) and experimental (hollow symbols and grey line) data. The radial profiles were extracted at $z/D = 5.5$ (black squares) and $z/D = 6.75$ (red circles).

in the top-right of the figure, plotting the radial slip velocity profile extracted at $z/D = 6$. The profile exhibits the sharp increase in W_{slip} at the boundary of the plume (around $r/D = \pm 1$ at this depth). This is followed by a mainly constant value (W_{slip} oscillates around 22 cm/s) inside the bubble column. The profile exhibits a top-hat distribution.

Fig. 9 presents the evolution in time of the vertical component of the dimensionless interfacial forces acting on a particular bubble along its track within the plume for 2000 time steps. The buoyancy force F_G is a straight horizontal line as no mechanism of mass transport was incorporated for the dispersed phase and the density is constant. There is a dynamic equilibrium when F_G , the main driving force, is counteracted by the drag force F_D . For a given bubble size, this equilibrium is achieved at a specific slip velocity (see Eq. (7)). In the present case, this equilibrium value is around $W_{slip} \approx 22$ cm/s as is shown in Fig. 8. The added mass term F_A is an inertial force that reacts to the fluctuations on F_D , but on average is an order of magnitude lower than F_D . Similarly for the fluid stress force F_S which does not appear to have a big impact on the total force. The lift force F_L , which is the result of the motion in the horizontal plane, is three orders of magnitude lower than the drag force.

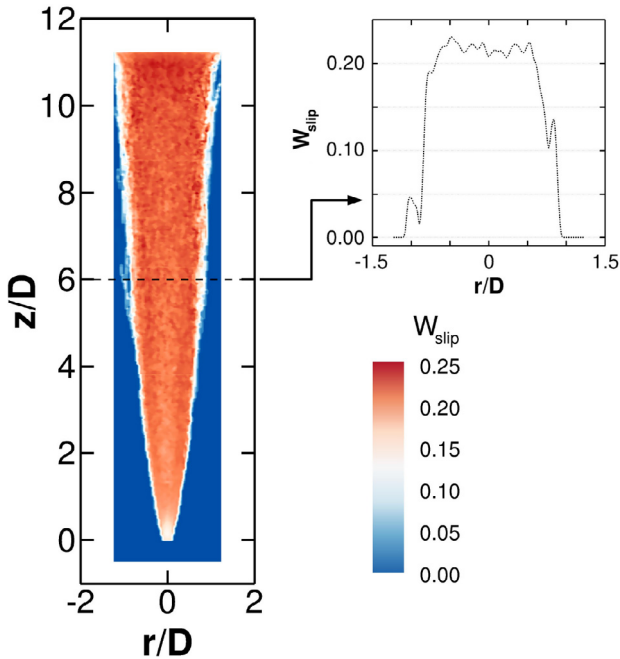


Fig. 8. Time-averaged vertical slip velocity field on a vertical plane that crosses the center of the plume (left) and extracted radial profile at $z/D = 6$ (right).

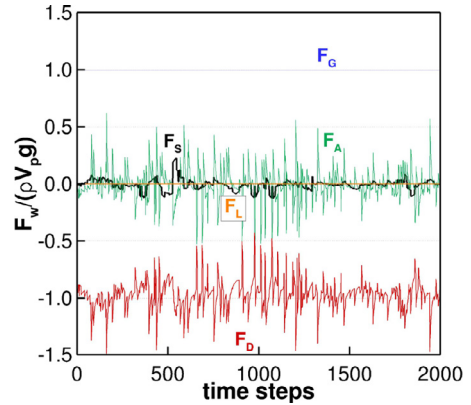


Fig. 9. Time series of the vertical component of the interfacial forces over a single bubble within the plume: buoyancy force (blue), added mass force (green), fluid stress force (black), drag force (red) and lift force (orange). The quantities are scaled with the buoyancy force for a theoretical bubble of zero density.

4.4. Sensitivity to $D_p/\Delta x$

First of all it should be noted that the time-averaged streamwise velocity distribution is insensitive to the grid resolution and this is not shown for brevity. Fig. 10 presents profiles of the numerically predicted second order statistics on the three meshes defined in Table 1 demonstrating the influence of $D_p/\Delta x$ on the turbulence quantities predictions. For the sake of clarity, only the numerical profiles at elevation $z/D = 6.75$ are plotted.

The profiles of the simulations on the coarse (circles) and medium (solid line) meshes are almost identical, exhibiting very little sensitivity to the chosen resolution. However, mesh refinement above Milelli’s limit (dashed line) appears to deteriorate the predictions. The smaller filter-width of the finer mesh does not help in capturing the eddies generated at (or below) the bubble scale. Additionally, the plume’s width scale b_v predicted by the finer mesh is higher, probably because of a better definition of the shear layer and the structures in the interface between the plume and the rest of the tank. As a result, the same number of particles have to trigger turbulence over a wider plume, resulting in the underprediction of the turbulent fluctuations.

4.5. Flow structure

The water flow in the tank is illustrated with the help of Fig. 11, which displays 3D streamlines of the time-averaged flow colored with the streamwise velocity in a quarter of the tank (and including the entire bubble plume). Three basic hydrodynamic elements are featured:

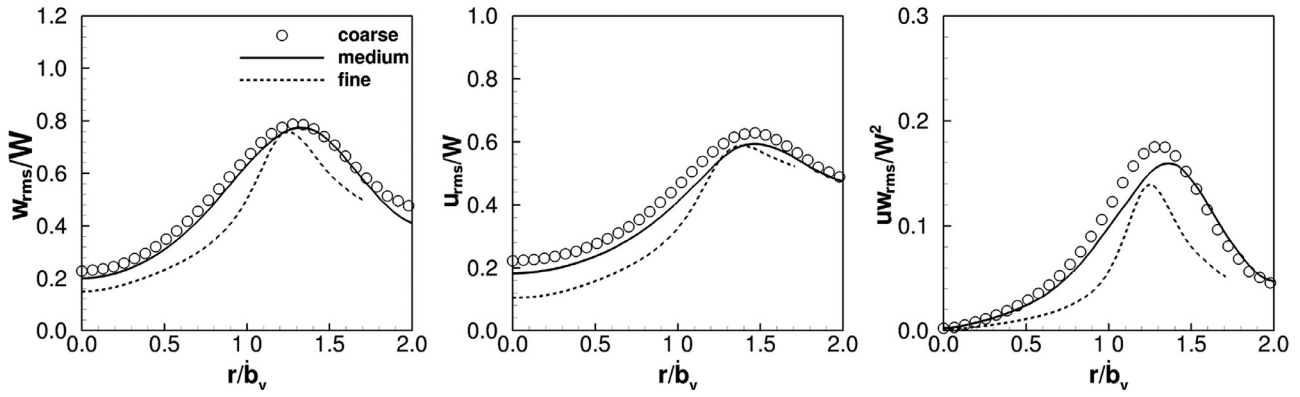


Fig. 10. Numerical profiles of the Turbulent Reynolds stresses for for the three grid resolutions on Table 1 at $z/D = 6.75$.

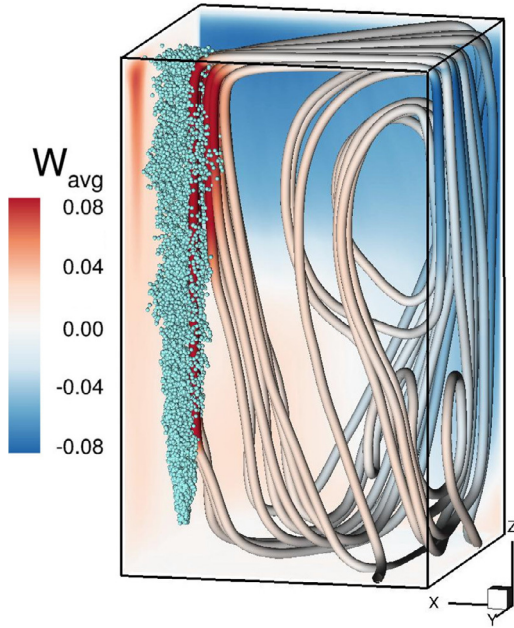


Fig. 11. Three-dimensional view of one quarter of the tank including the bubble plume and the streamtraces defining the secondary circulation.

1. the plume itself: as bubbles move upwards fluid is entrained thereby creating a high-momentum vertical fluid flow towards the water surface.
2. the returning flow: once the fluid reaches the water surface it spreads laterally towards the walls before it moves back down, thereby creating a large recirculation in the radial plane that dominates the top half of the tank.

3. three-dimensionality: whilst the plume is radially symmetric about the centreline of the tank, the tank itself is not and hence the distance from the plume to the wall is maximal in the diagonal direction. This means that the fluid has to fill the low momentum in corners (see Fig. 12, left) and hence it flows down faster in the corners of the tank thereby creating an imbalance of momentum in the horizontal plane. This momentum imbalance leads to a vortex/cell in a plane parallel to the walls in the lower third of the tank.

The twisted double-vortex structure is similar to a number eight shape with the two loops in perpendicular planes. The upper vortex is larger and exhibits higher velocity magnitudes than the lower one. The horizontal plane of the tank has four planes of symmetry and hence there are eight twisted double-cell structures as the one described in Fig. 11. Fig. 12 (left), presents contours of the time-averaged vertical velocity in a horizontal plane near the water surface and it shows how the high-momentum fluid from the plume is convected primarily to the corners of the tank. Fig. 12 (right) shows contours of the time-averaged vertical velocity in a radial plane and displays the plume and the upper cells of returning flow. The orientation of the axis of recirculation changes from radial for the upper loop of the "eight" to wall-parallel for the lower loop.

Finally, an instantaneous snapshot of the plume dynamics at two different instants in time are provided in Fig. 13 which depicts isosurfaces of the Q-criterion, an appropriate tool to visualize coherent structures from large-eddy simulations (Rodi et al., 2013). The isosurfaces are color-coded with the streamwise velocity. Coherent structures in the form of horseshoe vortices are visible at edge of the plume. The vortices are generated in the shear layer as a result of the large radial gradient of streamwise velocity in the radial direction indicated by the low velocities (blue color) at the edge of the plume. These structures start out as tubes around the plume. The slight wandering and unsteadiness of the plume restricts their extent in the circumferential direction to an angle of 30–90°.

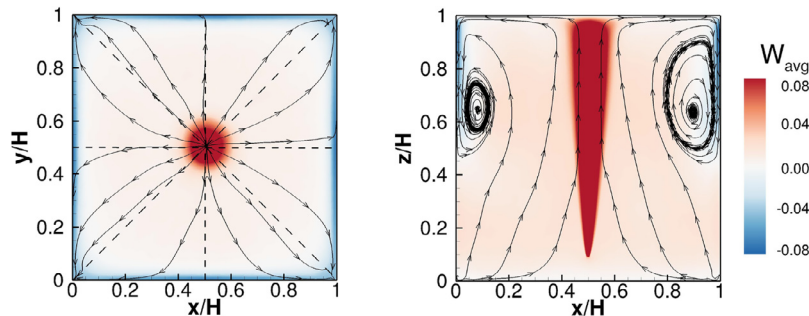


Fig. 12. Time-averaged vertical velocity contours on a horizontal plane close to the surface (left) and a vertical plane at the half of the tank (right).

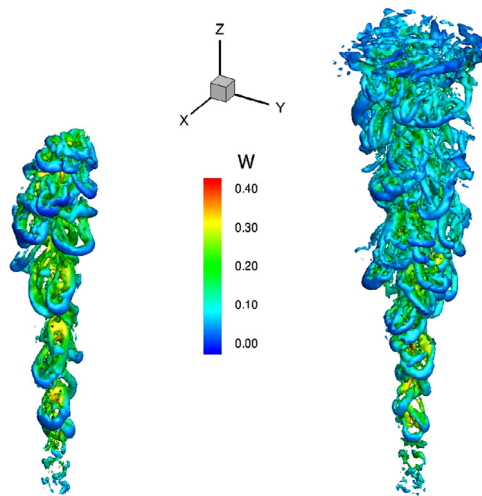


Fig. 13. Q-criterion isosurfaces for a developing column (left, $t = 5s$) and a fully-developed plume (right, $t > 20s$).

The continuous upwards movement of the plume convects the tubes vertically upwards, but due to the radial velocity gradient they are gradually stretched and result in the form of a horseshoe vortex. The different concentrations of bubbles and velocity fluctuations inside the plume generates some lateral inclination of the horseshoe vortices. The figure on the left depicts the plume at a very early stage and the radial gradients are stronger resulting in bigger and better defined vortices. When the plume is fully established (figure on the right) it covers a larger volume and the structures are more numerous and thinner. Vortices are shed into the returning flow where they dissipate very quickly.

5. Conclusions

A refined numerical methodology for large-eddy simulations of bubble plume dynamics is presented. It incorporates a new mapping algorithm which utilizes second-order smoothed delta functions as the interpolation technique for the forward coupling. It also suggests the use of a dynamic radius dependent on the $D_p/\Delta x$ ratio to define the influence volume where the bubble/node interaction takes place with minimum mesh-dependence.

The method has been validated using data from laboratory experiments carried out at Texas A&M University of a solitary bubble plume in an initially quiescent cubic water tank. The predicted stream-wise time-averaged velocities of the entrained liquid in the plume show a very good agreement with the experimental data and the theoretical curve.

This work presents some novel results on the model's capacity to solve the turbulent scales of motion on the continuous phase entrained in the plume. The numerical predictions of second-order statistics were satisfactory regarding the turbulent stresses trend and the fluctuations anisotropic nature. But while the agreement is remarkable for the horizontal fluctuations and the shear stress, the streamwise turbulence fluctuations are under-predicted in the core of the plume and its periphery. This may indicate some limitations in solving turbulent structures below the bubble length-scale. This issue does not seem to be a matter of lack of resolution as three different mesh resolutions were tested. The model proves to be mesh-independent until the threshold suggested by Milleli's condition, beyond which the simulation quality deteriorates. This indicates that Eulerian–Lagrangian assumptions prevent it from capturing smaller turbulent scales beyond a given mesh resolution. The authors suggest further research to include bubble-induced turbulence generation in the LES subgrid-scale closure.

The LES data have revealed interesting quantities that experiments cannot provide: For instance the vertical slip velocity between the two phases has been quantified and its distribution in the plume approximates a top-hat distribution. The average slip velocity for a given bubble size is mainly determined by the equilibrium between the buoyancy and drag forces. The added mass force appears to play an important role in balancing the oscillations of the drag component.

The analysis of the secondary flow has revealed the presence of a double-cell recirculating structure that dominates the flow in the tank. It is characterized by one large vortex at the radial plane that dominates the upper part of the tank and one smaller cell at the wall plane on the lower part. This bottom cell is a product of the momentum unbalance generated by the geometry itself. As the entrained water leaves the plume its trajectory turns towards the tank corners creating a shear flow. Finally, unsteady horse-shoe-type vortices generated at the edge of the plume are identified by visualization of the instantaneous flow field.

Acknowledgements

This research was supported by the BP/The Gulf of Mexico Research Initiative via the Gulf Integrated Spill Research Consortium (GISR). The numerical and experimental data presented in this paper are publicly available through the BP/Gulf of Mexico Research Initiative, GRIIDC database, in <http://ezid.cdlib.org/id/doi:10.7266/N76W980Z> (numerical code/parameters) and in <http://ezid.cdlib.org/id/doi:10.7266/N7BP00QT> (experimental ADV dataset). This work was performed using the computational facilities of the Advanced Research Computing @ Cardiff (ARCCA) Division, Cardiff University.

References

- Asaeda, T., Imberger, J., 1993. Structure of bubble plumes in linearly stratified environments. *J. Fluid Mech.* 249, 35–57. <http://dx.doi.org/10.1017/S0022112093001065>
- Bai, J., Fang, H., Stoesser, T., 2013. Transport and deposition of fine sediment in open channels with different aspect ratios. *Earth Surf. Process. Landf.* 38 (6), 591–600.
- Becker, S., De Bie, H., Sweeney, J., 1999. Dynamic flow behaviour in bubble columns. *Chem. Eng. Sci.* 54 (21), 4929–4935. [http://dx.doi.org/10.1016/S0009-2509\(99\)00214-6](http://dx.doi.org/10.1016/S0009-2509(99)00214-6)
- Becker, S., Sokolichin, A., Eigenberger, G., 1994. Gas-liquid flow in bubble columns and loop reactors: Part II. Comparison of detailed experiments and flow simulations. *Chem. Eng. Sci.* 49 (24), 5747–5762. [http://dx.doi.org/10.1016/0009-2509\(94\)00290-8](http://dx.doi.org/10.1016/0009-2509(94)00290-8)
- Bestion, D., 2012. Applicability of two-phase cfd to nuclear reactor thermalhydraulics and elaboration of best practice guidelines. *Nucl. Eng. Des.* 253, 311–321. <http://dx.doi.org/10.1016/j.nucengdes.2011.08.068>
- Bombardelli, F.A., Buscaglia, G.C., Rehmann, C.R., Rincón, L.E., García, M.H., 2007. Modeling and scaling of aeration bubble plumes: A two-phase flow analysis. *J. Hydraul. Res.* 45 (5), 617–630.
- Bomminayuni, S., Stoesser, T., 2011. Turbulence statistics in an open-channel flow over a rough bed. *J. Hydraul. Eng.* 137 (11), 1347–1358.
- Bryant, D.B., Seol, D.G., Socolofsky, S.A., 2009. Quantification of turbulence properties in bubble plumes using vortex identification methods. *Phys. Fluids* 21, 075101.
- Bunner, B., Tryggvason, G., 2002. Dynamics of homogeneous bubbly flows part 1. Rise velocity and microstructure of the bubbles. *J. Fluid Mech.* 466, 17–52. <http://dx.doi.org/10.1017/S0022112002001179>
- Caulfield, J., Adams, E., Auerbach, D., Herzog, H., 1997. Impacts of ocean CO2 disposal on marine life: II. Probabilistic plume exposure model used with a timevarying doseresponse analysis. *Environ. Model. Assess.* 2 (4), 345–353. <http://dx.doi.org/10.1023/A:1019081915826>
- Clift, R., Grace, J.R., Weber, M.E., 1978. *Bubbles, Drops and Particles*. Academic Press, New York.
- Crowe, C.T., Sharma, M.P., Stock, S.D.E., 1977. The Particle-Source-In cell (PSI-cell) model for gas-droplet flows. *J. Fluids Eng.* 99 (2), 325–332.
- Darmana, D., Deen, N., Kuipers, J., 2006. Parallelization of an EulerLagrange model using mixed domain decomposition and a mirror domain technique: application to dispersed gasliquid two-phase flow. *J. Comput. Phys.* 220 (1), 216–248. <http://dx.doi.org/10.1016/j.jcp.2006.05.011>
- Deen, N., van Sint Annaland, M., Kuipers, J., 2004. Multi-scale modeling of dispersed gasliquid two-phase flow. *Chem. Eng. Sci.* 59 (8–9), 1853–1861. <http://dx.doi.org/10.1016/j.ces.2004.01.038>
- Deen, N., Solberg, T., Hjertager, B., 2001. Large Eddy Simulation of the gasliquid flow in a square cross-sectioned bubble column. *Chem. Eng. Sci.* 56 (21–22), 6341–6349. [http://dx.doi.org/10.1016/S0009-2509\(01\)00249-4](http://dx.doi.org/10.1016/S0009-2509(01)00249-4)
- Delnoij, E., Lammers, F., Kuipers, J., van Swaij, W., 1997. Dynamic simulation of dispersed gas-liquid two-phase flow using a discrete bubble model. *Chem. Eng. Sci.* 52 (9), 1429–1458. [http://dx.doi.org/10.1016/S0009-2509\(96\)00515-5](http://dx.doi.org/10.1016/S0009-2509(96)00515-5)

- Dhotre, M.T., Deen, N.G., Ničeno, B., Khan, Z., Joshi, J.B., 2013. Large eddy simulation for dispersed bubbly flows: a review. *Int. J. Chem. Eng.* 2013, 1–22. <http://dx.doi.org/10.1155/2013/343276>
- Dhotre, M.T., Ničeno, B., Smith, B.L., Simiano, M., 2009. Large-Eddy Simulation (LES) of the large scale bubble plume. *Chem. Eng. Sci.* 64 (11), 2692–2704. <http://dx.doi.org/10.1016/j.ces.2009.02.040>
- Esmaeili, A., Tryggvason, G., 1998. Direct numerical simulations of bubbly flows. Part 1: low Reynolds number arrays. *J. Fluid Mech.* 377, 313–345. <http://dx.doi.org/10.1017/S0022112098003176>
- Fabregat, A., Dewar, W.K., Özgökmen, T.M., Poje, A.C., Wienders, N., 2015. Numerical simulations of turbulent thermal, bubble and hybrid plumes. *Ocean Modell.* 90, 16–28 (this issue). <http://dx.doi.org/10.1016/j.ocemod.2015.03.007>
- Hirt, C.W., Nichols, B.D., 1981. Volume-of-fluid (VOF) method for the dynamics of free boundaries. *J. Comput. Phys.* 39, 201–225.
- Hu, G., Celik, I., 2008. Eulerian–Lagrangian based Large-Eddy simulation of a partially aerated flat bubble column. *Chem. Eng. Sci.* 63 (1), 253–271. <http://dx.doi.org/10.1016/j.ces.2007.09.015>
- Hurth, D., Lemmin, U., 2001. A correction method for turbulence measurements with a 3D acoustic doppler velocity meter. *J. Atmos. Ocean. Technol.* 18, 446–458.
- Kara, S., Stoesser, T., Sturm, T.W., 2012. Turbulence statistics in compound channels with deep and shallow overbank flows. *J. Hydraul. Res.* 50 (5), 482–493.
- Kara, S., Stoesser, T., Sturm, T.W., Mulahasan, S., 2015. Flow dynamics through a submerged bridge opening with overtopping. *J. Hydraul. Res.* 53 (2), 282–294.
- Kim, D., Kim, J.H., Stoesser, T., 2013. The effect of baffle spacing on hydrodynamics and solute transport in serpentine contact tanks. *J. Hydraul. Res.* 51 (5), 558–568.
- Kim, S., Stoesser, T., 2011. Closure modeling and direct simulation of vegetation drag in flow through emergent vegetation. *Water Resour. Res.* 10 (47), W10511
- Kitagawa, A., Murai, Y., Yamamoto, F., 2001. Two-way coupling of Eulerian–Lagrangian model for dispersed multiphase flows using filtering functions. *Int. J. Multiph. Flow* 27 (12), 2129–2153. [http://dx.doi.org/10.1016/S0301-9322\(01\)00040-4](http://dx.doi.org/10.1016/S0301-9322(01)00040-4)
- Lai, C.K.C., 2015. An Analysis of Bubble Plumes in Unstratified Stagnant Water. Texas A&M University, p. 205 Phd thesis.
- Láin, S., Bröder, D., Sommerfeld, M., Göz, M., 2002. Modelling hydrodynamics and turbulence in a bubble column using the EulerLagrange procedure. *Int. J. Multiph. Flow* 28 (8), 1381–1407. [http://dx.doi.org/10.1016/S0301-9322\(02\)00028-9](http://dx.doi.org/10.1016/S0301-9322(02)00028-9)
- Lu, J., Fernández, A., Tryggvason, G., 2005. The effect of bubbles on the wall drag in a turbulent channel flow. *Phys. Fluids* 17 (9), 95–102. <http://dx.doi.org/10.1063/1.2033547>
- Ma, T., Ziegenhein, T., Lucas, D., Krepper, E., Fröhlich, J., 2014. Large Eddy simulations for dispersed bubbly flows. *CFD4NRS-5, Zürich*, 56. Switzerland, pp. 51–59.
- Martínez Mercado, J., Chehata Gomez, D., van Gils, D., Sun, C., Lohse, D., 2010. On bubble clustering and energy spectra in pseudo-turbulence. *J. Fluid Mech.* 650, 287–306. <http://dx.doi.org/10.1017/S0022112009993570>
- Mazzitelli, I., Lohse, D., 2009. Evolution of energy in flow driven by rising bubbles. *Phys. Rev. E* 79 (6), 1539–3755. <http://dx.doi.org/10.1103/PhysRevE.79.066317>
- Milelli, M., Smith, B., Lakehal, D., 2001. Large-Eddy Simulation of Turbulent Shear Flows Laden with Bubbles. Springer Netherlands. http://dx.doi.org/10.1007/978-94-017-1263-7_55. Direct and Large-Eddy Simulation IV, Vol. 8 of ERCOFTAC Series, 461–470
- Ničeno, B., Boucker, M., Smith, B.L., 2009. Euler-Euler Large Eddy Simulation of a square cross-sectional bubble column using the neptune-CFD code. *Sci. Technol. Nucl. Install.* 2009 Article ID 410272. <http://dx.doi.org/10.1155/2009/410272>
- Papanicolaou, A.N., Kramer, C.M., Tsakiris, A.C., Stoesser, T., Bomminayuni, S., Chen, Z., 2012. Energy spectra and bubble velocity distributions in pseudo-turbulence: numerical simulations vs. experiments. *Acta Geophys.* 60 (6), 1502–1546.
- Rodi, W., Constantinescu, G., Stoesser, T., 2013. Large-Eddy Simulation in Hydraulics. CRC Press, Taylor & Francis Group.
- Roghair, I., Mercado, J.M., Sint Annaland, M.V., Kuipers, H., Sun, C., Lohse, D., 2011. Energy spectra and bubble velocity distributions in pseudo-turbulence: numerical simulations vs. experiments. *Int. J. Multiph. Flow* 37 (9), 1093–1098. <http://dx.doi.org/10.1016/j.ijmultiphaseflow.2011.07.004>
- Sahoo, G.B., Luketina, D., 2003. Modeling of bubble plume design and oxygen transfer for reservoir restoration. *Water Res.* 37 (2), 393–401. [http://dx.doi.org/10.1016/S0043-1354\(02\)00283-X](http://dx.doi.org/10.1016/S0043-1354(02)00283-X)
- Sato, Y., Sekoguchi, K., 1975. Liquid velocity distribution in two-phase bubble flow. *Int. J. Multiph. Flow* 2 (1), 79–95. [http://dx.doi.org/10.1016/0301-9322\(75\)90030-0](http://dx.doi.org/10.1016/0301-9322(75)90030-0)
- Socolofsky, S.A., Adams, E.E., 2002. Multi-phase plumes in uniform and stratified crossflow. *J. Hydraul. Res.* 40 (6), 661–672. <http://dx.doi.org/10.1080/00221680209499913>
- Socolofsky, S.A., Adams, E.E., 2003. Liquid volume fluxes in stratified multiphase plumes. *J. Hydraul. Eng.* 129 (11), 905–914. [http://dx.doi.org/10.1061/\(ASCE\)0733-9429\(2003\)129:11\(905\)](http://dx.doi.org/10.1061/(ASCE)0733-9429(2003)129:11(905))
- Socolofsky, S.A., Adams, E.E., 2005. Role of slip velocity in the behavior of stratified multiphase plumes. *J. Hydraul. Eng.* 131 (4), 273–282. [http://dx.doi.org/10.1061/\(ASCE\)0733-9429\(2005\)131:4\(273\)](http://dx.doi.org/10.1061/(ASCE)0733-9429(2005)131:4(273))
- Socolofsky, S.A., Bhaumik, T., Seol, D.G., 2008. Double-plume integral models for near-field mixing in multiphase plumes. *J. Hydraul. Eng.* 134 (6), 772–783.
- Sokolichin, A., Eigenberger, G., Lapin, A., Lübert, A., 1997. Dynamic numerical simulation of gas-liquid two-phase flows Euler/Euler versus Euler/Lagrange. *Chem. Eng. Sci.* 52 (4), 611–626. [http://dx.doi.org/10.1016/S0009-2509\(96\)00425-3](http://dx.doi.org/10.1016/S0009-2509(96)00425-3)
- Stoesser, T., 2014. Large-eddy simulation in hydraulics: Quo vadis? *J. Hydraul. Res.* 52 (4), 441–452. <http://dx.doi.org/10.1080/00221686.2014.944227>
- Sungkorn, R., Derksen, J., Khinast, J., 2011. Modeling of turbulent gasliquid bubbly flows using stochastic Lagrangian model and Lattice–Boltzmann scheme. *Chem. Eng. Sci.* 66 (12), 2745–2757. <http://dx.doi.org/10.1016/j.ces.2011.03.032>
- Sussman, M., Smereka, P., Osher, S., 1994. A level-set approach for computing solutions to incompressible two-phase flow. *J. Comput. Phys.* 114, 146–159.
- Unverdi, S.O., Tryggvason, G., 1992. A front-tracking method for viscous incompressible, multi-fluid flows. *J. Comput. Phys.* 100, 25–37.
- Wüest, A., Brooks, N.H., Imboden, D.M., 1992. Bubble plume modeling for lake restoration. *Water Resour. Res.* 28 (12), 3235–3250. <http://dx.doi.org/10.1029/92WR01681>
- Yabe, T., Xiao, F., Utsumi, T., 2001. The constrained interpolation profile method for multiphase analysis. *J. Comput. Phys.* 169, 556–593.
- Yang, X., Zhang, X., Li, Z., He, G.-W., 2009. A smoothing technique for discrete delta functions with application to immersed boundary method in moving boundary simulations. *J. Comput. Phys.* 228 (20), 7821–7836. <http://dx.doi.org/10.1016/j.jcp.2009.07.023>
- Yapa, P.D., Zheng, L., Nakata, K., 1999. Modeling underwater oil/gas jets and plumes. *J. Hydraul. Eng.* 125 (5), 481–491. [http://dx.doi.org/10.1061/\(ASCE\)0733-9429\(1999\)125:5\(481\)](http://dx.doi.org/10.1061/(ASCE)0733-9429(1999)125:5(481))
- Yujie, Z., Mingyan, L., Yonggui, X., Can, T., 2012. Three-dimensional volume of fluid simulations on bubble formation and dynamics in bubble columns. *Chem. Eng. Sci.* 73, 55–78. <http://dx.doi.org/10.1016/j.ces.2012.01.012>